MIT Open Access Articles

Modeling of plasticity and fracture behavior of X65 steels: seam weld and seamless pipes

Modeling of plasticity and fracture behavior of X65 steels: Seam weld and Seamless pipes

Marcelo Paredes[1], Junhe Lian[2], Tomasz Wierzbicki[1], Mihaela E. Cristea[3], Sebastian Münstermann[2], Philippe Darcis[3]

[1]Impact and Crashworthiness Laboratory, Massachusetts Institute of Technology, Cambridge MA 02139, USA.
[2]Steel Institute, RWTH Aachen University, Intzestrasse 1, 52072 Aachen, Germany.
[3]TenarisDalmine S.p.A., Piazza Caduti 6 Luglio 1944, 1, 24044 Dalmine (BG), Italy.

Abstract

A non-associated/associated flow rule coupled with an anisotropic/isotropic quadratic yield function is presented to describe the mechanical responses of two distinct X65 pipeline steels. The first as a product of the cold-rolling forming (UOE) process also known as seam weld pipes and the second as a result of high temperature piercing process called seamless tube manufacturing. The experimental settings consist of a wide range of sample types, whose geometric characteristics represent different state of stresses and loading modes. For low to intermediate stress triaxiality levels, flat specimens are extracted at different material orientations along with notched round bar samples for high stress triaxialities. The results indicate that despite the existing differences in plasticity between materials due to anisotropy induced processes, material failure can be characterized by an isotropic weighting function based on the Modified Mohr-Coulomb (MMC) criterion. The non-associated flow rule allows for inclusion of strain directional dependence in the definition of equivalent plastic strain by means of scalar anisotropy (Lankford) coefficients and thus keeping the original capabilities of the MMC model.

1. Introduction

Pipeline network is one of the largest man-made structures ever built to transport goods from natural reservoirs to several receivers within the energy markets (Tubb, 2001). More than 65% out of the total amount of the worldwide line pipe infrastructure is installed only in the U.S., which includes onshore installations (processing plants, storages and distributors) and remote offshore facilities (subsea platforms, FPSO, etc.) (Ronalds, 2005; CIA, 2014). The material from which these pipes are made demands on meeting the stringent design requirements to withstand severe operating conditions and harsh environments. The most common materials naturally selected by pipe manufacturers are steel alloys due to their adequate mechanical reliability and economic feasibility. Pipeline steels are generally classified as different grades according to their mechanical properties and standardized according to their usage purposes by the industry as pipeline steel X series (Institute, 2007). Among the variety of X series pipes, X65 is widely used for high-pressure oil/gas transportation in either onshore or offshore facilities, based on the required flow rate and expected volume production. These expectations will dictate, not only, the outer diameter (D) and thickness (t), but also the manufacturing process from which the pipe will be produced for a given project. For instance, in deep water applications involving diameters less than 12 in seamless pipe is preferred over its longitudinally welded (seam weld) counterpart because weldments are usually viewed as weak spots, vulnerable to failure and corrosion (Guo *et*

al., 2014). As mentioned before, pipes may be manufactured by two traditional processes: cold-forming UOE and seamless. Cold-forming pipe production (UOE) tends to introduce intense strain gradients into the sheet at different directions relative to a fixed orthogonal coordinate system during formability, being the more severe those developed along the transverse direction. This not only affects the yield strength but also strain hardening and subsequent instability (necking), which finally are the driving forces behind initiation and propagation of fracture (Herynk *et al.*, 2007; Hara *et al.*, 2009, 2011; Arakawa *et al.*, 2013). On the other hand, the seamless pipe process yields a product with enhanced mechanical properties due to the heat treatment involved, which removes residual stresses and reduces ovality in the final shape. Consequently, the mechanical properties of the final product are expected to be spatially and directionally homogeneous.

Over the past years, the community has been working extensively on developing new types of constitutive models to predict anisotropic behavior in different materials. In the seminal work of Hill (Hill, 1949), anisotropy is introduced by means of a quadratic yield function with the directional dependence introduced in the form of six constants. Along with an associated flow rule to further the amount of plastic strain increment, this model predicts satisfactorily mechanical behavior of many types of metals. In the advent of a new generation of high strength steels (HSS), this yield criterion has fallen short in predicting ductility and plastic flow in finite strain settings. This has motivated a number of improvements of the original model where additional capabilities have been inserted over the years with successful results (Suh, Saunders and Wagoner, 1996; Rivalin *et al.*, 2000; Tsuru *et al.*, 2008; Iizuka, Hashimoto and Kuwabara, 2014; Iob, Campanelli and Coppola, 2015). Meanwhile, from the fundamental work of Barlat et al. (Barlat, Lege and Brem, 1991) and Karafillis and Boyce (Karafillis and Boyce, 1993), various non-quadratic yield functions have been developed to accounting for anisotropy in many materials such as aluminum and steel alloys. As a natural extension of large deformation, damage accumulation and subsequent failure eventually occurs at the material point. The fracture process usually involves a void growth mechanism of second phase particles such as carbides and inclusions embedded in the matrix material under plastic straining (Broek, 1973; Van Stone *et al.*, 1985; Garrison and Moody, 1987). Under isotropic assumptions, particles are uniformly distributed across the net section and its debonding -this is caused by applied remote loading-from the matrix material is directionally independent. But, experimental studies of Benzerga et al. (A. . Benzerga, Besson and Pineau, 2004; A. A. Benzerga, Besson and Pineau, 2004a, 2004b) show the initial porosity and that void aspect and void spacing ratios are quite sensitive to the fiber texture orientation produced in technological forming processes. From the micromechanics point of view, Bron and Besson (Bron and Besson, 2004) proposed a phenomenological yield function to represent plastic anisotropy based on linear transformations of Cauchy stress tensor. It turns out that the non-quadratic function coupled with a micromechanical GTN (Gurson-Tvergaard-Needleman) fracture model produces satisfactory results in predicting directional dependency of plastic flow (strain hardening) but fail in predicting fracture propagation (Tanguy *et al.*, 2008). It means that ductile facture mechanism is also influenced by the surrounding matrix and possibly by the distribution of inclusions (Benzerga and Besson, 2001; A. . Benzerga, Besson and Pineau, 2004; A. A. Benzerga, Besson and Pineau, 2004b). A further refinement of

2

this work proves that accounting for anisotropy in the evolution of a porous media subjected to plastic straining yields satisfactory outcomes not only in fracture initation but also in propagation at different loading directions (Morgeneyer *et al.*, 2009; Shinohara, Madi and Besson, 2016).

A parallel line of research involving a phenomenologically-based failure criteria have emerged over the past decades, which establishes that the macro crack occurrence is a result of irreversible plastic damage accumulation process. As a result, the global mechanical response (load-displacement curve) all the way to fracture is modelled as an independent functional relation of plasticity and fracture. In that sense, yield condition and subsequent plastic flow is uncoupled from the failure phenomenon, which enables further modifications of the current model capabilities. For instance, Qian et al. (Qian et al. 2016; Qian et al. 2017) introduced in two different publications non-quadratic and quadratic yield equations with non-associated plastic flow, respectively, to describe yielding and hardening response in aluminum alloys with an isotropic fracture model. It turns out that despite the anisotropic nature exhibited by 6xxxx series alloys, the fracture prediction under invariant directional settings yields an acceptable engineering solution to the problem of shear punch tests. This is possible only if the loading axis is aligned to one of the principal axes of anisotropy at which the calibrated model parameters are obtained under associated flow rule assumption. A rather different scenario is viewed when multi-axial loading conditions act on anisotropic materials, the initiation of fracture becomes highly directional dependent and the simple isotropic assumption may not hold true if normality condition is imposed. In recent studies, Luo et al. and Gu & Mohr (Luo et al. 2012; Gu & Mohr 2015) proposed a phenomenological fracture criterion based on a linear transformation of the von Mises equivalent plastic strain definition to take account for anisotropy under complex state of stresses at distinct material orientations. A more recent investigation on anisotropic fracture mechanism in metal sheets, Jia and Bai (Jia and Bai, 2016) proposed a functional angular form to characterize different stress states and loading modes in the principal strain space in terms of linearly transformed equivalent plastic strain.

In the current work, a simple non-associated flow rule coupled with a quadratic anisotropic yield function is presented to predict plastic behavior of the material at different loading directions. By means of the Lankford coefficients and stress ratios directionally measured from experiments, the initial yield stress and further plastic flow are determined. The directional dependency of the material is introduced in the non-associated equivalent plastic strain definition and thus keeps the isotropic nature of the Modified Mohr-Coulomb (MMC) from which is based to predict failure. The experimental settings consist of a wide range of geometry types, whose particular characteristics represent different states of stresses and loading modes. For low to intermediate stress triaxiality levels, flat specimens are extracted at different material orientations. Likewise, notched round bar samples are also extracted to characterize high stress triaxiality levels. The studied materials are two X65 pipeline steels coming from different manufacturing processes: seam weld and seamless. The evidence shows that keeping the original features of Hill's yield criterion, strain hardening induced anisotropy can be captured by non-associated flow rule assumption. This approach exploits the potentiality of the so-called Lankford parameters to describe the intrinsic mechanical properties of the plastic straining phenomenon.

2. Experimental Program

The experimental program is comprised by a number of tensile and shear tests on different types of specimen geometries at various loading orientations. Details of the testing procedure as well as material description is outlined as follow.

2.1. Materials

A selected set of two X65 pipeline steels were prepared for the current study to determine plasticity and fracture characteristics needed to calibrate the present constitutive model. Specimens were machined out from cut pipe sections. Outer and inner surfaces of the pipe were remove and only the core was kept as a prismatic block whose height was 80% of the pipe thickness. The X65 Seamless (SL) and Seam weld (SW) pipes possess a heavy wall-thickness t of 40mm and 19mm with outer diameter OD of 406mm ($D/t \sim 10$) and 610mm ($D/t \sim 32$), respectively. The pipe sections were cut at 12:00 position for SL and 9:00 position for SW. Particularly, in the latter the selected section was away from the fusion zone (weld line). A number of sheets were sliced down to accommodate the flat specimens aligned in different directions by means of Electrical Discharge Machine (EDM) and the remaining material block was kept for round bar samples manufacturing as depicted in Fig. 1. The outer profile of all samples were initially cut with a water jet cutter machine, and later the hard edges were smoothed with the CNC milling process. The final thickness for the batch of flat specimens was 2.5mm for X65-SW and 2.0mm for X65-SL. The notched round bars and special shear flat specimens kept the same final dimensions in both materials. The chemical composition of these materials are given in Table 1.

Table 1 Chemical composition of X65 pipeline steels.

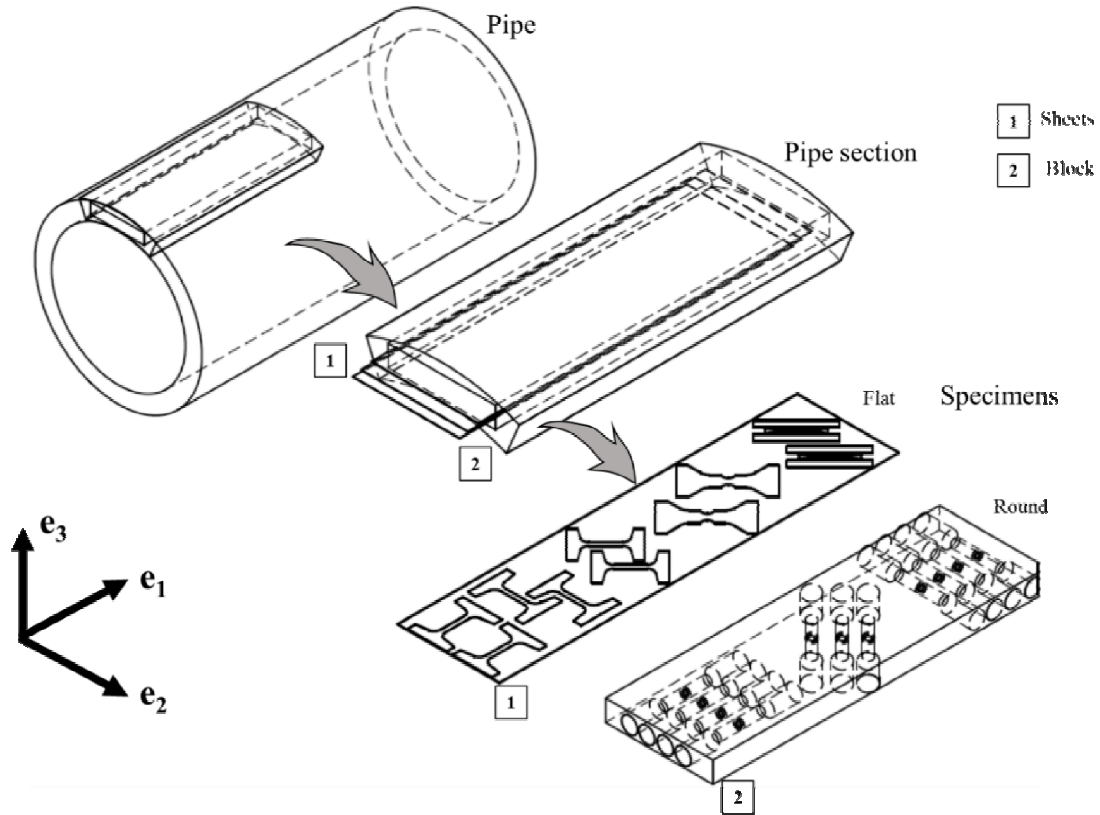| Material	C %	Si %	Mn %	P %	S %	Cr %	Mo %	Ni %	Al %	Cu %
X65-SL	0.070	0.260	1.000	0.010	<0.001	0.390	0.340	0.290	0.030	0.080
X65-SW	0.056	0.313	1.510	0.009	<0.001	0.152	0.019	0.082	0.026	0.051

Fig. 1 Conceptual sketch of X65 pipeline steel extraction process for sampling.

2.2. Testing procedure

A comprehensive set of tensile, shear and biaxial compression tests were performed to characterize mechanical behavior of the materials along different orientations and a wide range of stress states. For such purposes, the characterization is divided in two parts: plasticity and fracture (damage). Plasticity is considered the response of the material to large deformation (finite strain) including post-necking stage and is measured by means of uniaxial tensile "Dog Bone" tests (DB, see Fig. 2). DB specimens were extracted along three different directions (0°, 45° and 90°) with respect to longitudinal axis of the pipe to quantify material orientation dependency (anisotropy) as well as hardening response. All uniaxial tensile specimens were loaded at the same cross-head velocity of 0.5mm/min by means of a universal testing machine. A random speckle pattern with an average speckle size of about 200 μm is spread on the specimen surface and records at a frequency of 1Hz using Retiga 1800i camera with a resolution of 25 pixels per mm. The strain and displacement fields were measured and computed using the Digital Image Correlation (DIC) system with virtual extensometers placed along the axial gage length and width of specimens. The vertical extensometer lengths for uniaxial tensile tests and flat samples (NT20, NT10, NT6.67 and CH) were 12mm and 30mm, respectively, whereas for notched round bar and shear specimens the extensometer length was 10mm and 2mm, respectively. The Lankford ratios are defined as the ratio of the plastic width strain to plastic

5

thickness strain along the three selected directions, $r_\alpha = \frac{d\varepsilon_w^p}{d\varepsilon_{th}^p}$ (see Fig. 3b). The evolution of plastic width strain is obtained by using virtual extensometer whose length is equivalent to width dimension (6mm) and the plastic thickness strain is calculated assuming the principle of plastic incompressibility.
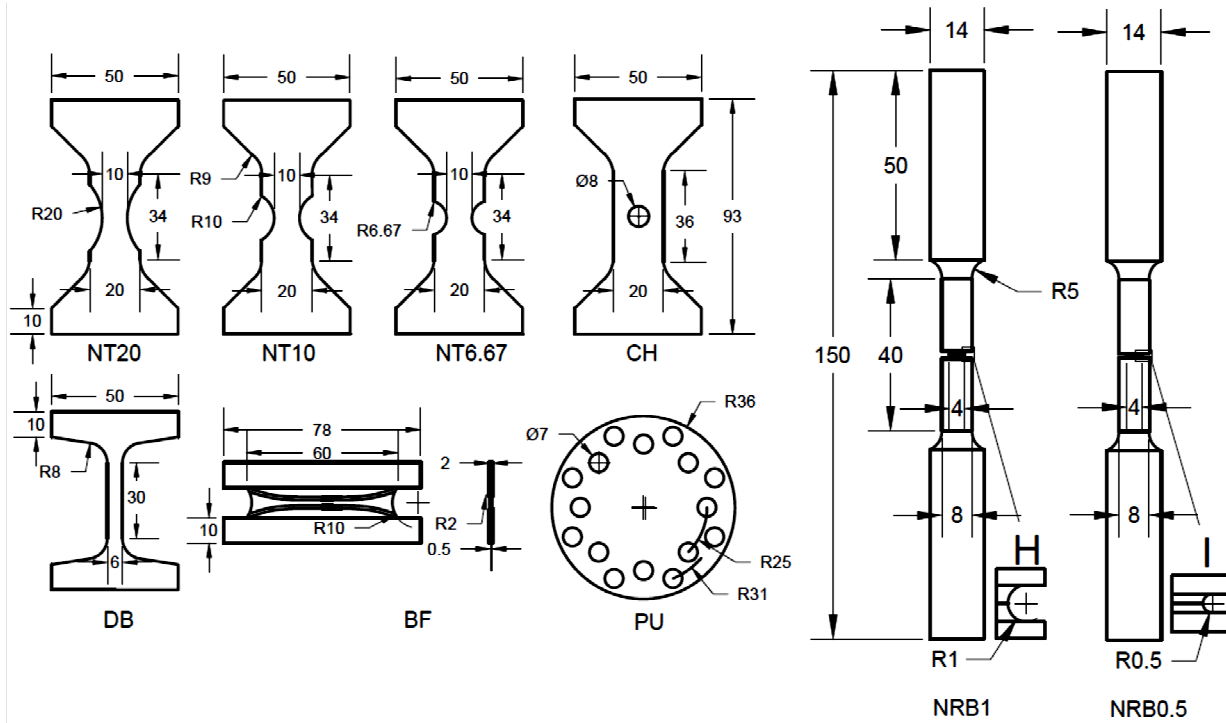

Fig. 2 Specimen geometries for testing procedure (dimensions in mm): Uniaxial tensile flat bar (DB), notched tensile flat bars with different notch radii (NT20, NT10 and NT6.67), central hole with 8mm radius (CH), shear butterfly (BF), punch disk (PU) and notched tensile circular bars for different radii (NRB1 and NRB0.5). All dimensions are given in mm.

On the other hand, fracture initiation in the present study is regarded as the limit of ductility or the onset of damage, which describes the irreversible damage process of an ideal material point until failure. Special tensile-shear geometries serve to determine the stress state at which fracture initiation occurs. For that purpose, notched flat and round tensile bars with different radii, shear and punch disk specimens were tested. A clear distinction must be made between flat and round bar specimens and the limiting range at which the stress triaxiality might reach in each type of geometry. For instance, low-to-intermediate stress triaxialities ($\eta = 0 \sim 2/3$), tensile flat samples with double-circular edge cutouts (NT's), and central hollow (CH) specimens were employed in addition to the shear butterfly (BF) sample (Dunand and Mohr, 2011) and punch (PU) disk specimen. The latter represents plane-stress equi-biaxial tensile loading condition and is depicted in Fig. 2. Three distinct radii were carved on the NT samples in order to control the intensity of stress triaxiality inside the specimen: 20mm, 10mm, 6.67mm. The Instron dual-actuator testing apparatus allows for vertical and/or horizontal motion of the specimen's shoulders. Almost any loading condition between pure shear and transverse plane-strain tension can be reproduced in flat specimens. Both the vertical and the horizontal actuators can be either force or displacement

6

controlled. Residual forces due to grip tightening are eliminated by switching to force control in order to zero the force before the test begins.

For high stress triaxiality levels ($\eta > 1$), round bar specimens with radii of 1mm (NRB1) and 0.5mm (NRB0.5) were added. Similar speckles pattern was applied on the specimen surface to the one used for uniaxial tensile tests and DIC system for data recording. Tensile testing for notch round bar specimens and compression experiments for punch disks were performed in a MTS 200kN loading frame. The moving crosshead is driven by precision ball screws with a customized screw-thread fixture to prevent slippery at the sample ends during stretching. All experiments in this work were carried out under constant crosshead velocity of 0.5mm/min until fracture.

2.3. Experimental results

The uniaxial tensile tests on three material orientations, as shown in Fig. 3a, indicates that both materials exhibit almost identical elastic behavior at the beginning (albeit certain deviation) of the loading while in the elastic-plastic regime a remarkable difference is observed. Particularly, the X65-SL's hardening curve is preceded by a well-defined Luder's band ($\bar{\varepsilon} \sim 2\%$) compared to the "round-house" stress-strain curve shape of the X65-SW. However, yield and ultimate strengths of SL are closely related one to another with a difference about ~2% between the highest value and 0°, while SW displays well defined stress levels at each orientation having a deviation of about 7% with respect to the reference direction (0°) for yield and ultimate strengths. This apparent in-plane anisotropy may suggest a gradual development of preferred orientation of crystal planes as strain increases in which individual crystals become elongated to form a characteristic fibrous texture in the direction of the most severe tensile strain (Hill, 1949). Fig. 3b presents the evolution of the plastic strains of width vs. thickness for three material orientations. The slope of these curves serve the basis to compute the so-called Lankford coefficients (r_α), which is a practical engineering form to measure orientation dependency. A material can be considered isotropic when the Lankford ratios approach to unity and anisotropic when differs from it. Despite that $r_{0°} = 0.93$ for X65-SL, the material can be assumed to be isotropic since the $r_{45°}$ and $r_{90°}$ are nearly unity. Moreover, the X65-SW steel is completely anisotropic, as shown in Table 2.

Table 2 Mechanical properties of X65 pipeline steel

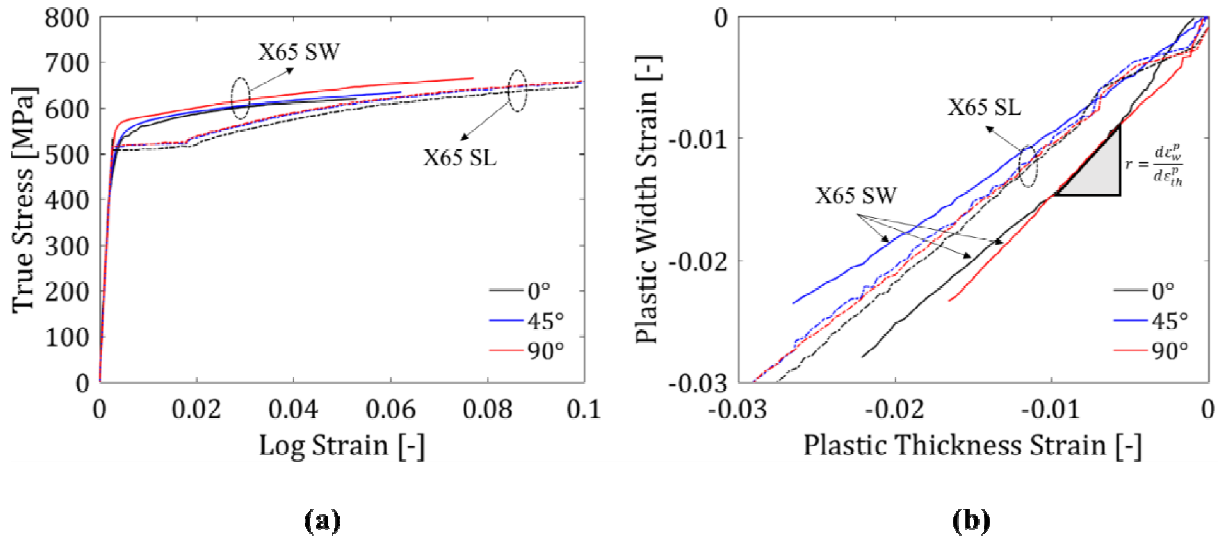| Material	E	v	σ_y	σ_{uts}	Elong.	Lankford
	GPa		MPa	MPa		r_α
X65-SL						
0°			507	647	0.28	0.93
45°	210	0.3	515	660	0.29	0.97
90°			516	659	0.25	0.98
X65-SW						
0°			530	620	0.22	0.77
45°	210	0.3	540	634	0.33	1.14
90°			568	665	0.29	0.70

Fig. 3 Mechanical behavior of both X65 pipeline steels (seam weld (SW) and seamless (SL)) at different material orientation: (a) True Stress-Log Strain curves; (b) Plastic width strain-plastic thickness strain curves.

Figs. 4 and 5 shows the measured force-displacement responses of both materials for each special geometries intended for fracture and plasticity characterization. In particular, the anisotropy behavior is well evident for X65-SW in Fig. 4 such that each plot accommodates the flow curves at different material orientation (0°, 45° and 90°) in colored solid lines. The solid mark (▼) indicates the displacement at which fracture initiation occurs as the point where the load drops sharply. This ad hoc assumption is permissible since the underlying model is based specifically on macroscopic observations and thus microcracks and its interaction with the matrix material are irrelevant. As Benzerga and Leblond (Benzerga and Leblond, 2010) stated that from uniaxial tensile tests of standard specimens two fracture strains can be measured: initiation and final failure. The latter is considered as total separation of specimen parts and is preceded by a short crack extension across the gage section. On the other hand, the former only occurs with the appearance of a macrocrack at the interior of the material which affect directly the global load-displacement evolution. In that sense, a staggering number of identical geometries for each configuration would be required to conduct interrupted tests all the way to fracture. After visual examination of fracture surfaces on break open specimens (post-mortem) a minimum size of a macrocrack might be defined as a result of damage accumulation in the material. There is still an open question about the size of the crack at which fracture initation is considered as such and its effect on the mesoscale level. Even though, multi-specimen technique might bring certain reliability on failure initation detection, the cost and limitations related to material availability make it disadvantageous.

Note that the effect of anisotropy on the material yield strength of tensile tests (see Figs. 4a to d) is more apparent along 90° (hoop direction) than other directions, but plastic flow curves decrease radically (strain softening) just after reaching the peak load at small elongations

(~0.5mm). While the strain hardening response of specimens loaded along 0° and 45° seems to flow parallel, the 90° sample response, otherwise, follows a completely different pattern by crossing over the other curves. A similar trend is observed in notched round bars (NRB). Despite small differences in yield strength and hardening behavior at various directions, the curves remains almost parallel all the way to fracture (see Figs. 4g and h). Moreover, the displacement to fracture appears to be affected by anisotropy. For instance, cracks initiate first in samples aligned with the hoop direction, then in samples along the reference (axial) axis and finally in specimens oriented to 45°. This behavior is consistently observed for all experiments with varying ductility level due to specimen severity (shape geometry). A rather different picture emerges for shearing test, where the loading configurations for axial and hoop direction are almost on top each other and follow a rising pattern, while diagonal configuration exhibits a less steep (plateau) flow curve preceded by the peak force (Fig. 4e). In addition to this, punch disk PU is included for biaxial stress state characterization. Digital image correlation, in particular, was not calibrated for these tests because the onset of fracture coincides with the instant of maximum load.

The load-deflection curves of X65-SL pipe steel for all experiments are plotted. Since the material exhibits isotropic behavior in all considered directions, only representative results are included. For the sake of the space and to facilitate the visual interpretation of the outcome, all flat tensile specimens are grouped in Fig. 5a, the notch round bars are grouped in Fig. 5b, the special butterfly shear specimens and punch disk are grouped in Fig. 5c and 5d, respectively. The force level is not comparable with X65-SW since the specimen thickness of flat geometries is different ($t = 2$mm) including punch disk. Meanwhile, the flow curves display a pronounced isochoric deformation (strain hardening) before the peak force is attained (~1.0mm), which denotes enhanced mechanical property compared to previous material. Figs. 5b and 5c correspond to NRB's and BF tests which have similar dimensions to their alternatives X65-SW (see Figs. 4e, 4g and 4h). Then, a qualitative comparison can be made: for notched round bars, the maximum forces and plastic flow trends are comparable between them, but ductility seems to be reduced for SW. Similar results are also observed in BF experiments (Figs. 4e and 5c), where the displacement to fracture (ductility) of X65-SL increases 25% in comparison to its alternative oriented in the axial direction.
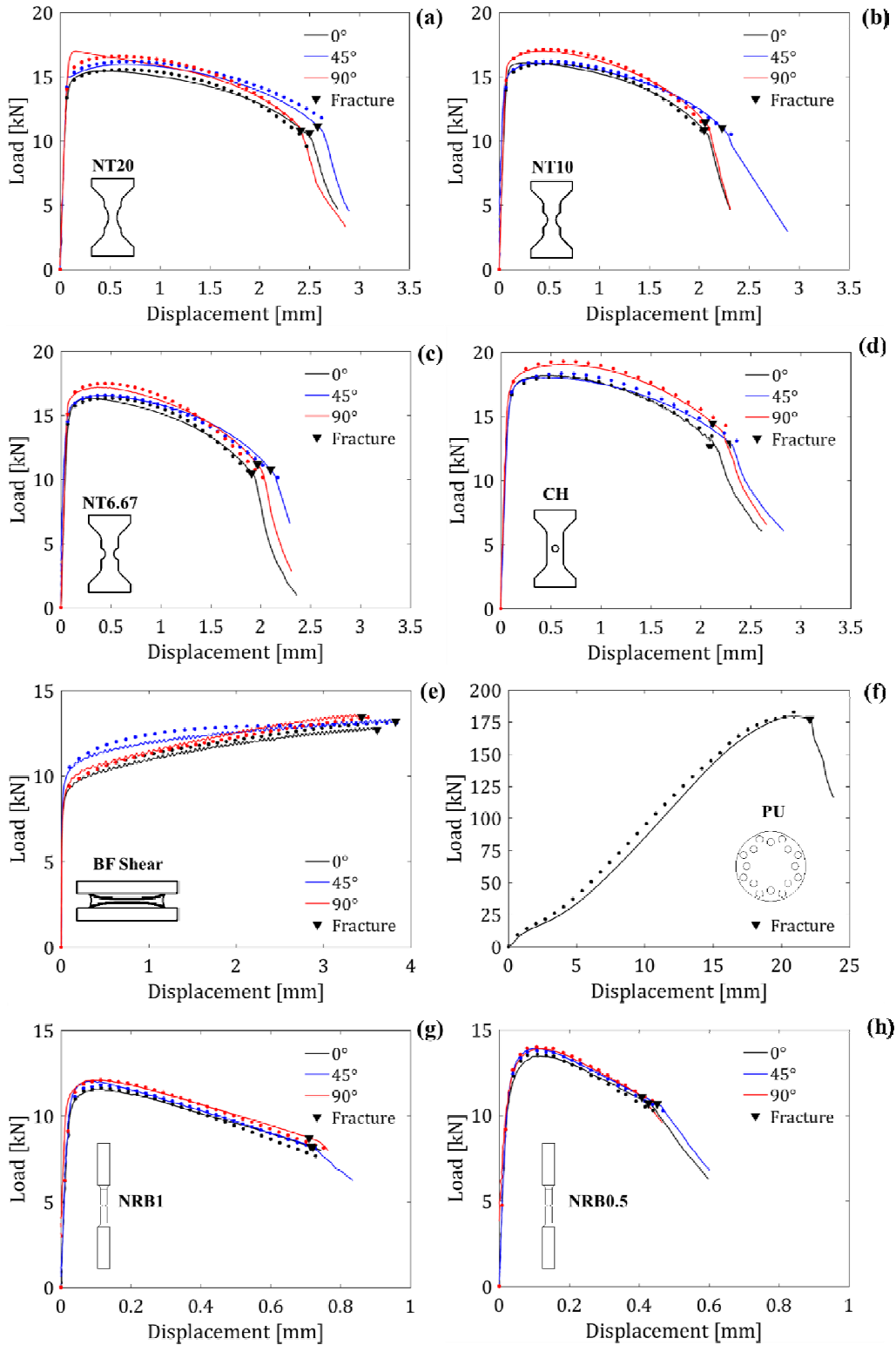
Fig. 4 Experimental results of X65-SW: (a) NT20, (b) NT10, (c) NT6.67, (d) CH, (e) BF, (f) PU, (g) NRB1 and (h) NRB0.5. Colored solid and dot lines represent experiments and numerical simulations (without damage), respectively. Solid marks (▼) are the measured fracture initiation points.
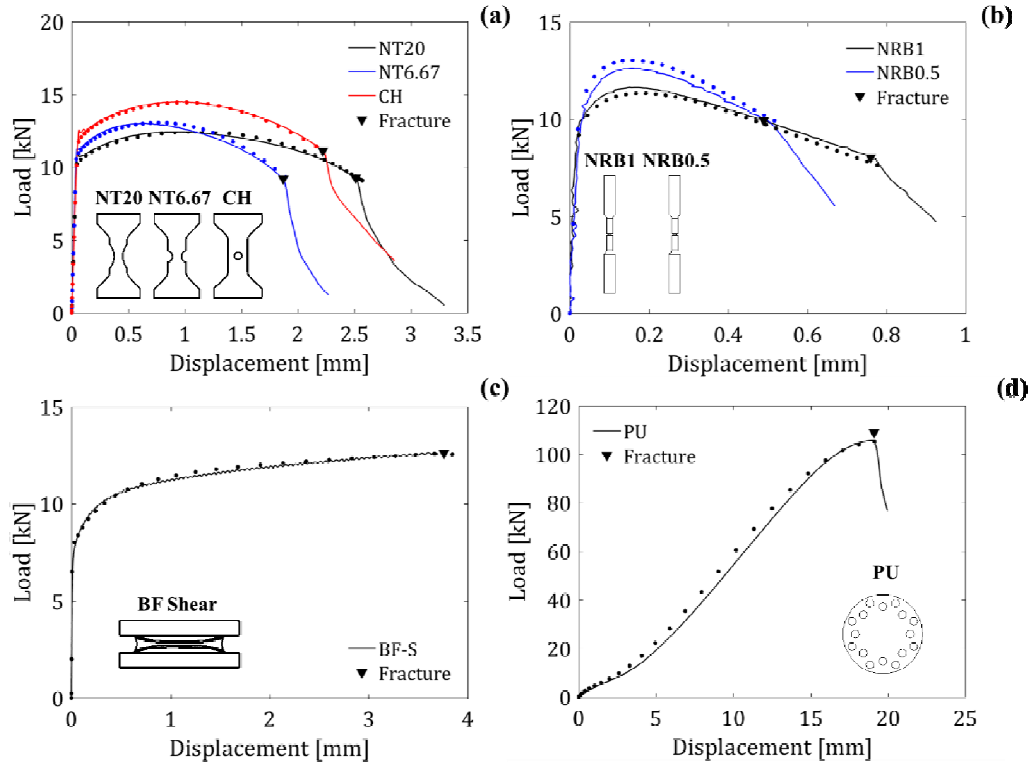
10

Fig. 5 Experimental results of X65-SL: (a) NT20, NT6.67 and CH; (b) NRB1 and NRB0.5; (c) BF and (d) PU. Colored solid and dot lines represent experiments and numerical simulations (without damage), respectively. Colored solid and dot lines represent experiments and numerical simulations (without damage), respectively. Solid marks (▼) are the measured fracture initiation points.

2.4. Microstructure examination

To provide a metallurgical understanding of the mechanical behavior of these two pipeline steels, the microstructure of them are studied by light optical microscopy (LOM) and scanning electron microscopy (SEM). Two important microstructural features are focused here, the matrix grain structure/size and the characteristics of inclusions, as both are contributing significantly to the final plasticity and toughness behavior of the pipe steels. The micrographs for the investigated two X65 steels are presented in Fig. 6, while the quantitative analysis of these features is shown in Table 3.

Based on the LOM and SEM micrographs, both steels indicate single-phase, bainitic microstructure, although the metallurgical production process for the two types of steels is quite different. It is well known from the scientific literature based on EBSD analysis, that this type of microstructure features a rich amount of low angle grain boundaries, and these boundaries are the natural barriers for the dislocation movements, which results in a good strength and toughness combination. To compare quantitatively, the grain size of the X65-SW is slightly smaller than X65-SL, as shown in Table 3. This also partially contributes to the higher yield

strength of the X65-SW in Fig. 2 due to the grain refinement hardening mechanism. Both steels reach a quite good impurity level with about 0.05% inclusions.
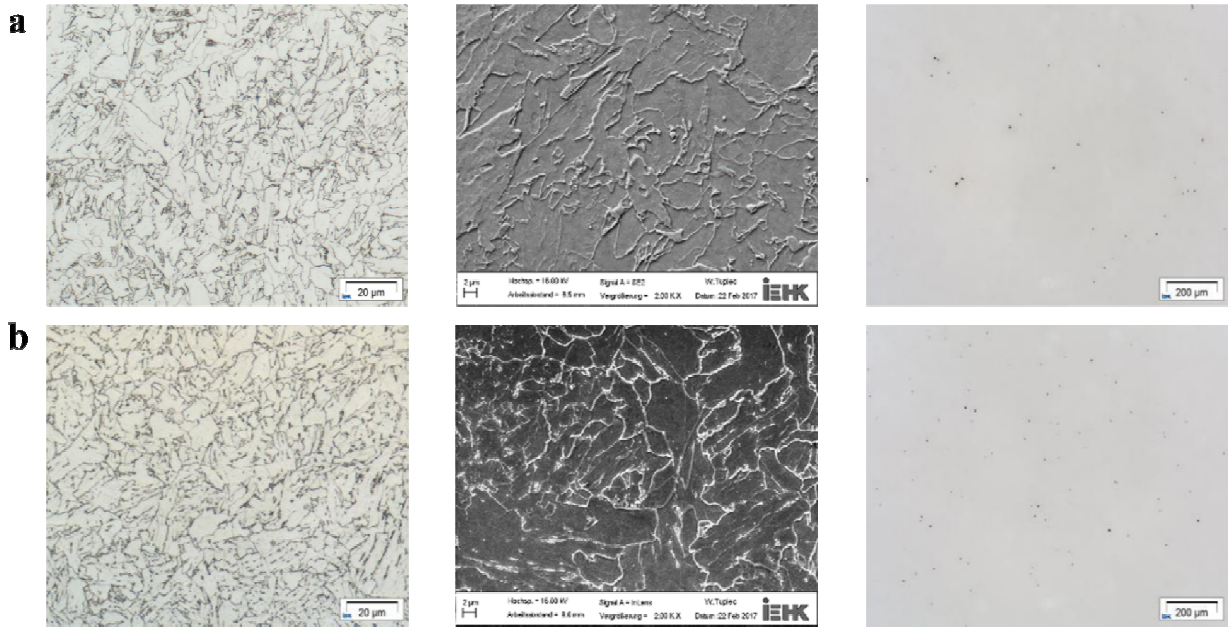

Fig. 6 Optical micrographs (left), scanning electron microscopy (SEM) images (center) and inclusion observation (right) of typical microstructure formed in manufacturing process for a) seam weld and b) seamless line pipe steels.

Table 3 Grain structure, grain size and the inclusion analysis of two X65 pipeline steels.

	Grain structure	Grain size		Inclusions		
		Average size	Standard deviation	Area fraction	Average size	Shape factor
X65-SL	Bainite	9.30 µm	2.61	0.045%	3.70 µm	0.96
X65-SW	Bainite	6.42 µm	2.12	0.050%	4.82 µm	0.88

3. Rate-independent plasticity model

3.1. Yield function

The mechanical behavior of both X65 pipeline steels is described by a simple quadratic yielding function in the form

$$f(\sigma, k) = \bar{\sigma} - k = \sqrt{(\mathbf{P}\boldsymbol{\sigma}) \cdot \boldsymbol{\sigma}} - k = 0 \tag{1}$$

where, $\boldsymbol{\sigma}$ and k represents the symmetric Cauchy stress tensor and deformation resistance, respectively. $\mathbf{P}$ is the semi-positive definite matrix of the material stress ratios measured at

different loading directions conveniently given in the following form (Mohr, Dunand and Kim, 2010)

$$\mathbf{P} = \begin{bmatrix} P_{11} & P_{12} & P_{31} & 0 & 0 & 0 \\ P_{12} & P_{22} & P_{23} & 0 & 0 & 0 \\ P_{31} & P_{23} & P_{33} & 0 & 0 & 0 \\ 0 & 0 & 0 & P_{44} & 0 & 0 \\ 0 & 0 & 0 & 0 & P_{55} & 0 \\ 0 & 0 & 0 & 0 & 0 & P_{66} \end{bmatrix} \tag{2}$$

The coefficients of $\mathbf{P}$ matrix are related to Hill's anisotropy coefficients as (Hill, 1949)

$$\begin{bmatrix} P_{11} \\ P_{22} \\ P_{33} \\ 2P_{12} \\ 2P_{23} \\ 2P_{31} \\ P_{44} \\ P_{55} \\ P_{66} \end{bmatrix} = \begin{bmatrix} G+H \\ F+H \\ F+G \\ -2H \\ -2F \\ -2G \\ 2N \\ 2M \\ 2L \end{bmatrix} \tag{3}$$

The expansion of the product in Eq. (1) will be set equal to Hill's equivalent stress

$$\bar{\sigma}^2 = (G+H)\sigma_{11}^2 + (F+H)\sigma_{22}^2 + (F+G)\sigma_{33}^2 - 2H\sigma_{11}\sigma_{22} - 2F\sigma_{22}\sigma_{33} - 2G\sigma_{11}\sigma_{33} + 2N\sigma_{12}^2 + 2M\sigma_{31}^2 + 2L\sigma_{23}^2 \tag{4}$$

rearranging Eq. (4) by assuming that the anisotropy is negligible in the out-of-plane shear components and the selected reference material orientation is along the longitudinal axis ($e_1.e_1$), the $\mathbf{P}$ matrix can be simplified significantly into three independent parameters, $\mathbf{P}_{12}$, $\mathbf{P}_{22}$ and $\mathbf{P}_{44}$

$$\mathbf{P} = \begin{bmatrix} 1 & P_{12} & -(1+P_{12}) & 0 & 0 & 0 \\ P_{12} & P_{22} & -(P_{22}+P_{12}) & 0 & 0 & 0 \\ -(1+P_{12}) & -(P_{22}+P_{12}) & 1+2P_{12}+P_{22} & 0 & 0 & 0 \\ 0 & 0 & 0 & P_{44} & 0 & 0 \\ 0 & 0 & 0 & 0 & 3 & 0 \\ 0 & 0 & 0 & 0 & 0 & 3 \end{bmatrix} \tag{5}$$

For the special case of the von Mises isotropic yield function is retrieved by setting $\mathbf{P}_{12} = -0.5$, $\mathbf{P}_{22} = 1$ and $\mathbf{P}_{44} = 3$.

3.2 Flow rule

The flow rule defines the amplitude of the increment plastic strain tensor in the appropriate stress space. Classical plasticity theory requires that the plastic strain increment lie normal to the yield surface as the stress derivative of function f (Eq. 1). This associate flow condition does not always hold true for all cases when anisotropy is present (Stoughton, 2002). Instead, a plastic potential function $\mathbf{g}$ is used to account for directional effect on plastic strain evolution in the form

$$d\varepsilon_p = d\lambda \frac{\partial \mathbf{g}}{\partial \boldsymbol{\sigma}} \tag{6}$$

where $d\lambda$ is nonnegative scalar multiplier while $\partial \mathbf{g}/\partial \boldsymbol{\sigma}$ is the gradient of the plastic potential from which plastic strain vector is computed. In the same fashion as before, $\mathbf{g}$ function is defined as a quadratic function in stress space

$$g(\boldsymbol{\sigma}) = \sqrt{(\mathbf{G}\boldsymbol{\sigma}) \cdot \boldsymbol{\sigma}} \tag{7}$$

where $\mathbf{G}$ is a positive definite matrix written in the following form

$$\mathbf{G} = \begin{bmatrix} 1 & G_{12} & -(1+G_{12}) & 0 & 0 & 0 \\ G_{12} & G_{22} & -(G_{22}+G_{12}) & 0 & 0 & 0 \\ -(1+G_{12}) & -(G_{22}+G_{12}) & 1+2G_{12}+G_{22} & 0 & 0 & 0 \\ 0 & 0 & 0 & G_{44} & 0 & 0 \\ 0 & 0 & 0 & 0 & 3 & 0 \\ 0 & 0 & 0 & 0 & 0 & 3 \end{bmatrix} \tag{8}$$

Note that in the special case of $\mathbf{P} = \mathbf{G}$ the associate flow rule is retrieved.

3.3 Isotropic hardening

In the context of non-associate flow rule, the combined Swift-Voce isotropic strain hardening describes the plastic flow behavior in agreement with experiments, even in the post-necking region

$$k(\bar{\varepsilon}_p) = \alpha A(\varepsilon_0 + \bar{\varepsilon}_p)^n + (1-\alpha)\left(k_0 + Q(1 - e^{-\beta\bar{\varepsilon}_p})\right) \tag{9}$$

where A, ε_0 and n are material parameters of Swift model and k_0, Q and β are coefficients of Voce equation. Through the α coefficient the contribution of each hardening model is weighted to determine the influence of the plastic work done (δw_p) on the material during each increment of plastic strain $(\delta \varepsilon_p)$. Then, due to the work-conjugate principle the equivalent plastic strain $(d\bar{\varepsilon}_p)$ is related to equivalent stress $(\bar{\sigma})$ in the form

$$\delta w_p \equiv \sigma : d\varepsilon_p = \bar{\sigma} d\bar{\varepsilon}_p \tag{10}$$

Thus, the relation between equivalent plastic strain and plastic multiplier is

14

$$d\bar{\varepsilon}_p = d\lambda \frac{g}{\sigma} \tag{11}$$

Which differs from the classical associate flow rule equation in which the plastic strain rate is equal the incremental plastic multiplier.

3.4 Model calibration

In this section the calibration procedure is outlined to adjust material parameters of the present model for X65 pipeline steels.

3.4.1 Quadratic function coefficients

The quadratic yield and plastic potential functions describe how the stress and strain components evolve during the plastic straining. Due to the convexity nature of these functions, their evolution is constrained by the plastic flow rule to increase as specified by the stress-strain relation obtained from uniaxial tensile tests. Since f and g belong to the family of homogeneous functions of degree unity (which implies that the locus merely expands without changing shape as the material hardens), the model parameters might only be adjusted using the first yield (0.2% offset proof stress) at different material orientation. Taking the yield stress along $0°$ as a reference, the first component of **P** matrix can be obtained as $P_{11} = 1$ (Eq.5). The remaining P_{ij} components are computed by fitting a set of linear equations (resolve Eq. 4 for each direction) with experimental data (stress ratios). On the other hand, G_{ij} are calculated in a more straightforward manner. Upon evaluating Eq. 6 in its plane stress version, the r_α values and **G** components can be related as

$$G_{12} = -\frac{r_0}{1+r_0} , G_{22} = \frac{r_0(1+r_{90})}{r_{90}(1+r_0)} \text{ and } G_{44} = \frac{(1+2r_{45})(r_0+r_{90})}{r_{90}(1+r_0)} \tag{12}$$

By generalizing anisotropic yield function in conjunction with the current flow rule, the Lankford ratio can be expressed in a continuous form with respect to the loading direction

$$r_\alpha = \frac{(G_{44}+2G_{12}-G_{22}-1)\sin^2\alpha \cos^2\alpha - G_{12}}{(1-G_{22})\cos^2\alpha + G_{12}+G_{22}} \tag{13}$$

as well as the direction-dependent yield stress is given as

$$\sigma_y^\alpha = \frac{k}{(\cos^4\alpha + (2P_{12}+P_{44})\sin^2\alpha \cos^2\alpha + P_{22}\sin^4\alpha)} \tag{14}$$

In case of non-directional dependency (isotropy), the von Mises yield function and associate flow rule are recovered by setting **P** = **G** as shown in Table 4. Fig. 7 shows the calibrated function for yielding and plastic flow for both associated and non-associated settings.

Table 4 Yield and plastic potential coefficients for X65 pipeline steels

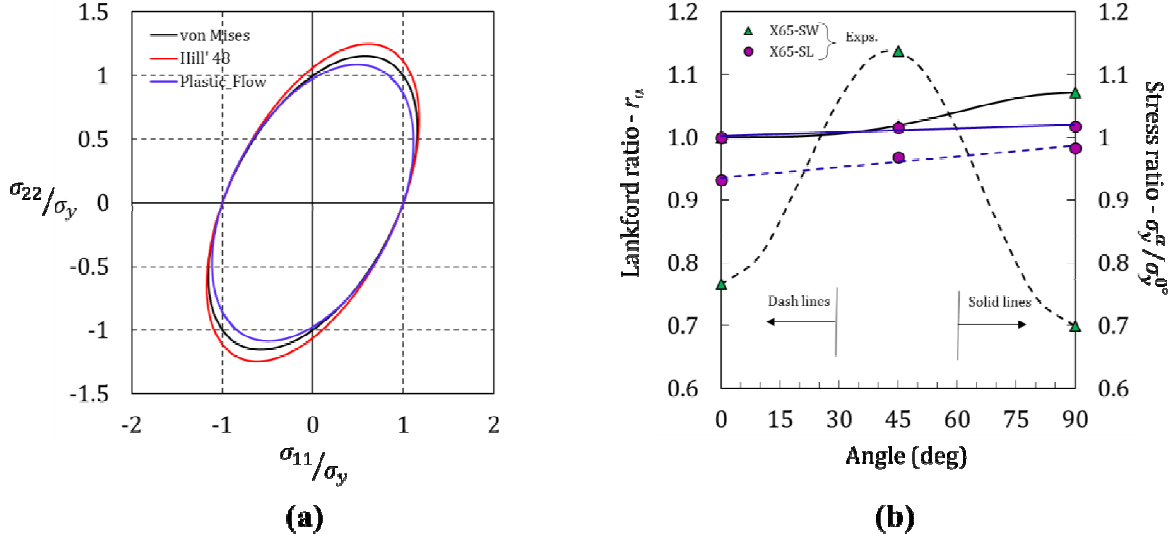|	P_{12}	P_{22}	P_{44}	G_{12}	G_{22}	G_{44}
X65-SL	-0.5	1	3	-0.5	1	3
X65-SW	-0.493	0.887	3.021	-0.451	1.051	3.681

Fig. 7 (a) 2D representation of quadratic yield functions and plastic potential in stress space; (b) angular evolution of r_α and σ_y^α values for X65 pipeline steels (symbols and colored dash/solid lines represent experiments and analytical solutions, respectively).

3.4.2 Post-necking behavior

The isochoric plastic deformation is well captured by uniaxial tensile tests all the way until the onset of necking (ultimate tensile strength) point. Beyond that a complex triaxial stress state develops inside the plastic zone making the data recording unreliable. As an alternative to overcome such limitation, the post-necking regime is then estimated by a hybrid experimental-numerical procedure, where the simulated load-displacement response is enforced to match with an experimental one by an iterative process (Ling, 2004). Here, an improved version is used by means of a weighting function that combines the potentiality of a power law (Swift) function with the versatility of an exponential type equation (Voce) given in Eq. 9. This scheme has proven to be effective for other types of materials, see illustrative examples in (Gu & Mohr 2015; Paredes et al. 2016; Abi Akl & Mohr 2017). Since isotropic hardening has been chosen, a specimen oriented in only one direction (reference) is needed to calibrate material parameters. A tensile flat specimen with double notches of 20mm radius (NT20) oriented along axial direction (0°) is loaded all the way to fracture. The measured load-displacement serves as a reference for the numerical iterative process to find a suitable weighting coefficient α. The procedure begins by fitting the material parameters of each type to the measured true stress-logarithmic plastic strain, up to ultimate tensile stress, separately. Then, a suitable 3D FE model is built of NT20 specimen geometry (see appendix A for details), whose initially fitted stress-strain data with a first guess of α serve as the starting point of the iterative process. This step is completely automated by an algorithm code which minimize an error function between the measured and simulated load-displacement results while varying α. The limiting cases of the proposed fitting scheme for post-necking response are: $\alpha = 0$, a fully exponential saturation type form is

16

obtained; $\alpha = 1$, a power law is recovered (Paredes *et al.*, 2017). Table 5 shows the calibrated material parameters for both X65 pipeline steels.

Table 5 Swift-Voce hardening law parameters for X65 pipeline steels

	A	ε_0	n	k_0	Q	β	α
X65-SL	991.19	0.028	0.2	483.04	223.74	13.95	0.3
X65-SW	722.35	0.001	0.054	526.25	93.95	53.24	1.4

The set of parameters given in Tables 4 and 5 forms part of the anisotropic non-associated constitutive model presented herein, aiming at to predict plastic flow and yielding in X65 steels. It can be seen that, from the calibration procedure outlined before, a reduced number of uniaxial tensile samples at different material orientation is suffice to determine the necessary constants required by Hill's quadratic function and Lankford ratios. These enable the construction of the yield and plastic flow locus (Fig. 6a) and directional material dependency (Fig. 6b) in the respective space. Likewise, the post-necking weighting coefficient α is obtained by an iterative process applied to a selected geometry. Figs. 4 and 5 display the numerical results of the load-displacement response (colored dotted lines) of all tested specimen geometries along with their experimental counterparts. These outcomes can be seen as validation in all loading orientation conditions, except NT20 along 0° which was used for calibration.

4. Isotropic fracture modeling

The Modified Mohr-Coulomb (MMC) phenomenological fracture criterion is used to describe fracture initation in X65 steels (Bai and Wierzbicki, 2010). The stress state based model allows to track the evolution of equivalent plastic strain all the way until the limit of ductility is reached in terms of the stress triaxiality (η) and the Lode angle ($\bar{\theta}$) (see Appendix B for details)

$$\hat{\varepsilon}_f(\eta, \bar{\theta}) = \left\{ \frac{A}{C_2} \left[C_3 + \frac{\sqrt{3}}{2-\sqrt{3}} (1 - C_3) \left(\sec\left(\frac{\bar{\theta}\pi}{6}\right) - 1 \right) \right] \left[\sqrt{\frac{1+C_1{}^2}{3}} \cos\left(\frac{\bar{\theta}\pi}{6}\right) + C_1 \left(\eta + \frac{1}{3}\sin\left(\frac{\bar{\theta}\pi}{6}\right) \right) \right] \right\}^{-\frac{1}{n}}$$

(15)

where A and n are the same material constants previously adjusted for the power law part of Eq. 9. Assuming that the stresses and strains are univocally mapped by a power law expression in the elastic-plastic regime, then the original stress based Mohr-Coulomb model is transformed into the mixed strain based space conveniently expressed in Eq. 15. Three facture independent parameters (c_1, c_2 and c_3) need to be calibrated from experiments. Consequently, the fracture initiation is achieved when the damage indicator D reaches unity

$$D(\bar{\varepsilon}_p) = \int_0^{\bar{\varepsilon}_f} \frac{d\bar{\varepsilon}_p}{\hat{\varepsilon}_f(\eta, \bar{\theta})}$$

(16)

17

where $d\bar{\varepsilon}_p$ is the effective plastic strain increment and $\bar{\varepsilon}_f$ is the strain to fracture as determined by the hybrid experimental-numerical procedure above described. Under monotonic loading conditions, it is expected to have proportionality not only at the force components acting on the specimen boundaries but also at the stress components acting on the material point (characteristic local stress state). In uniaxial tensile tests, mainly, characterized for plastic instability (diffuse necking) and subsequent fracture initation (localization), the local stress state evolves along with large plastic deformation due to changes in the specimen geometry. This necking-induced loading path variation, somehow, breaks down the fundamental assumption that the evolving load history must be constant all the way to fracture. For that reason, in order to overcome the setback originated by the loss of proportionality in some specimen geometries due to post-necking regime, the above Eq. 16 is utilized as averaging operator of the damage indicator to account for the effect of the non-proportional loading.

The non-associated equivalent plastic strain previously defined in Eq. 11 can be expanded into a functional relationship with plastic strain tensor

$$d\bar{\varepsilon}_p = \left(\tfrac{g}{\sigma}\right)^2 \sqrt{\left[\mathbf{P}\mathbf{G}^{-1}(d\varepsilon_p)\right] \cdot \mathbf{G}^{-1}(d\varepsilon_p)} \tag{17}$$

If $\mathbf{P} = \mathbf{G}$ the associated equivalent plastic strain is recovered in terms of Hill's quadratic yield condition for anisotropy media. Meanwhile, $\mathbf{P}_{12} = -0.5$, $\mathbf{P}_{22} = 1$ and $\mathbf{P}_{44} = 3$ yields the classical isotropic von Mises equivalent strain. Despite the recommendation, given by Bai and Wierzbicki (Bai and Wierzbicki, 2010), of using experiments that exhibit negligible load history dependency for calibration – i.e. BF_S, PU and NRB0.5 –, a non-proportional strain history specimen geometry is included – i.e. NT20 – to complete the parameters adjustment. All those oriented along the reference direction (longitudinal axis). Through the FE results, the loading history $(\eta, \bar{\theta})$ of the critical material point (presumably where fracture initiates) of each selected geometry is retrieved and then by enforcing Eq. 16 to be unity, the fracture parameters are calculated (Paredes, Wierzbicki and Zelenak, 2016). Table 6 indicates the calibrated parameters, while Fig. 8 shows the plots of the loading path to fracture for X65-SL. The open symbols represent the strain to fracture predicted by the current fracture criterion (Eq. 16), whereas the solid black lines are the loading history obtained from the FE simulations whose ends indicate the corresponding measured fracture point.

Table 6 MMC fracture parameters

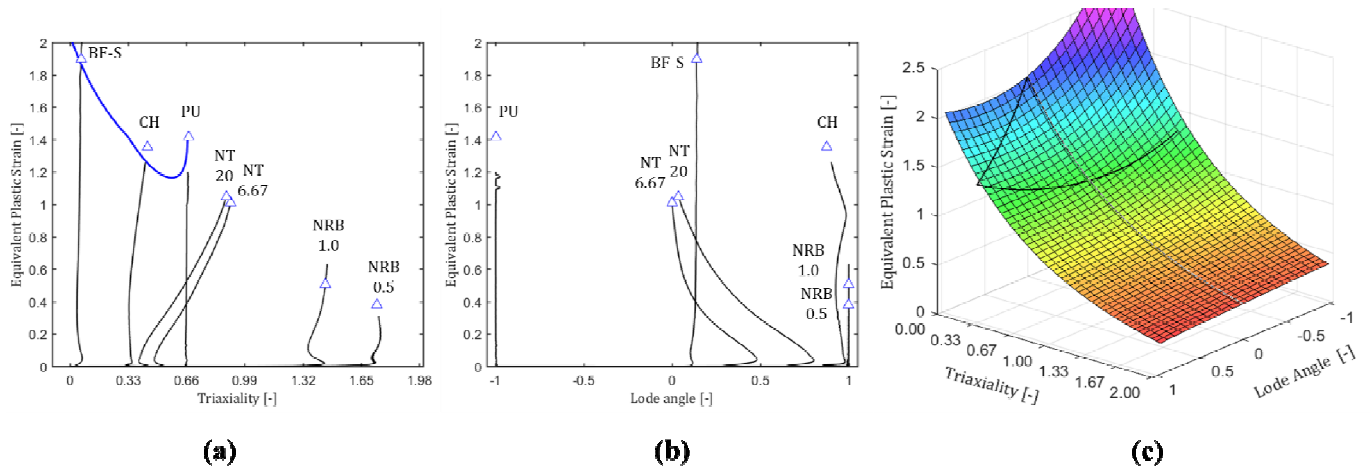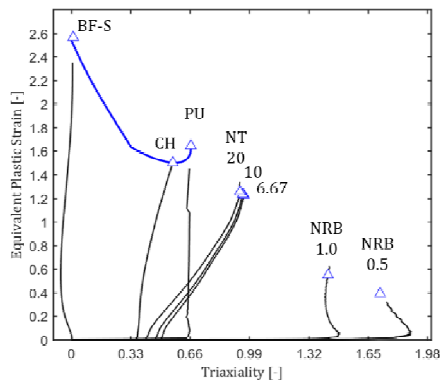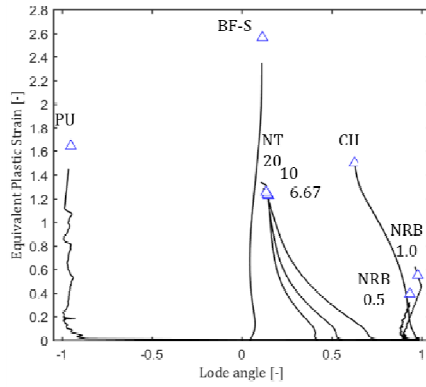|	c_1	c_2	c_3
X65-SL	0.12	598.44	0.90
X65-SW	0.029	381.77	0.87

Fig. 8 The loading history at critical material point of several specimen geometries for X65 seamless pipeline steels: (a) bi-dimensional visualization of strain to fracture versus stress triaxiality; (b) bi-dimensional visualization of strain to fracture versus Lode angle parameter; (c) Three dimensional fracture surface representation. The open triangle symbols correspond to the estimated fracture initiation point by the model, while the end of solid lines represent the strain to fracture determined through hybrid numerical-experimental analysis.

Likewise, the fracture envelopes for X65-SW at different direction with their respective loading history are plotted in Fig. 9. The surfaces were obtained from simulations using the calibrated parameters given in table 6, while the blue lines in Figs. 8a, 9a, 9d and 9g (black lines in Figs. 8c, 9c, 9f and 9i) represents the special state where the stress triaxiality is mapped one-to-one with the Lode angle in plane stress condition (Wierzbicki & Xue 2005; Bai & Wierzbicki 2008), see Appendix B for details. It can be seen that the surfaces for the three selected orientations are the same despite the loading path of each specimen differs one to another. The predicted value of strain to fracture (blue triangle) are in good agreement with those obtained from the hybrid experimental-numerical analysis (end of solid lines), mainly for tensile experiments (NT's, NRB's and CH). However, biaxial tensile test (PU) exhibits a lower measured ductility compared to the prediction in around ~15%.
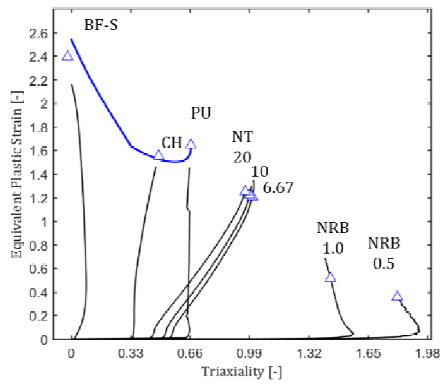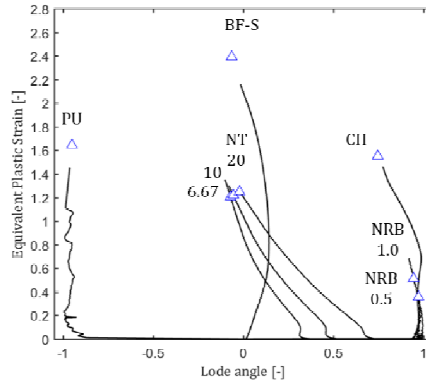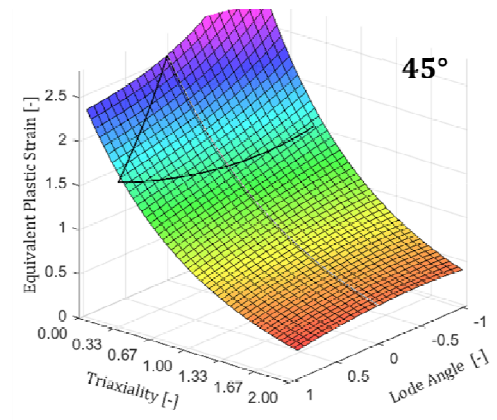
19
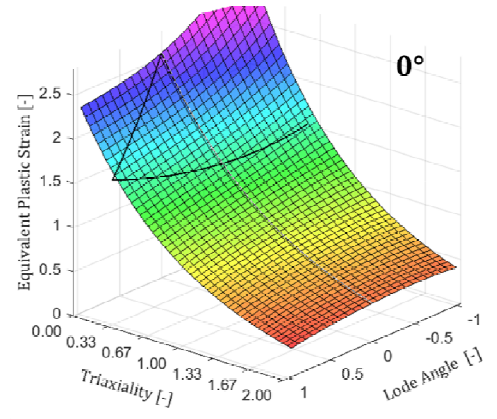
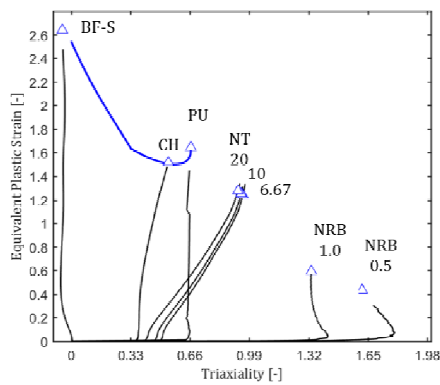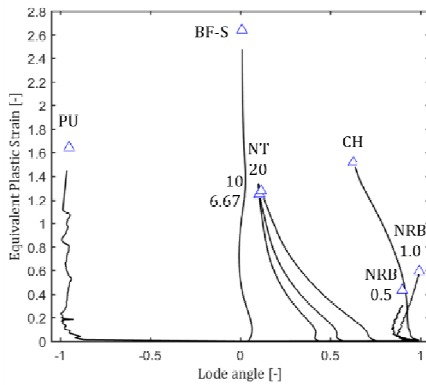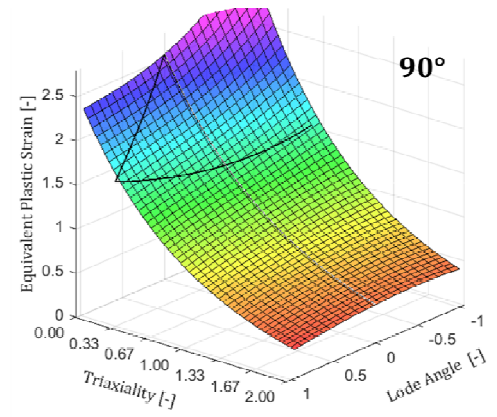**Fig. 9** The loading history at critical material point of several specimen geometries for X65 seam weld pipeline steels for different material orientations. First, second and third row corresponds to 0°, 45° and 90° orientation with respect to the reference direction. The open triangle symbols correspond to the estimated fracture initiation point by the model, while the end of solid lines represent the strain to fracture determined through hybrid numerical-experimental analysis.

5. Comparison of results

Fig. 10 shows a comparison of loading paths and fracture envelopes between seamless and seam weld pipes, oriented along the reference direction, of various selected specimen geometries. It can be seen that the fracture initiation point is strongly influenced by the stress state. As the stress triaxiality intensity decreases, the fracture point increases. The X65-SW is more ductile compared to its counterpart X65-SL. However, ductility for notched round bars diminishes gradually in almost the same proportion as the notch radius is reduced from 1mm to 0.5mm (~50%). But, at the same time, fracture initiation of both materials seems to be comparable. These results suggest that fracture is strongly influenced by the third stress invariant (Lode angle) when the stress triaxiality intensity decreases. On the contrary, the effect becomes negligible for triaxialities greater than unity ($\eta > 1$) as it is shown in Fig. 10b, where the surfaces flattened and almost overlapped one another.

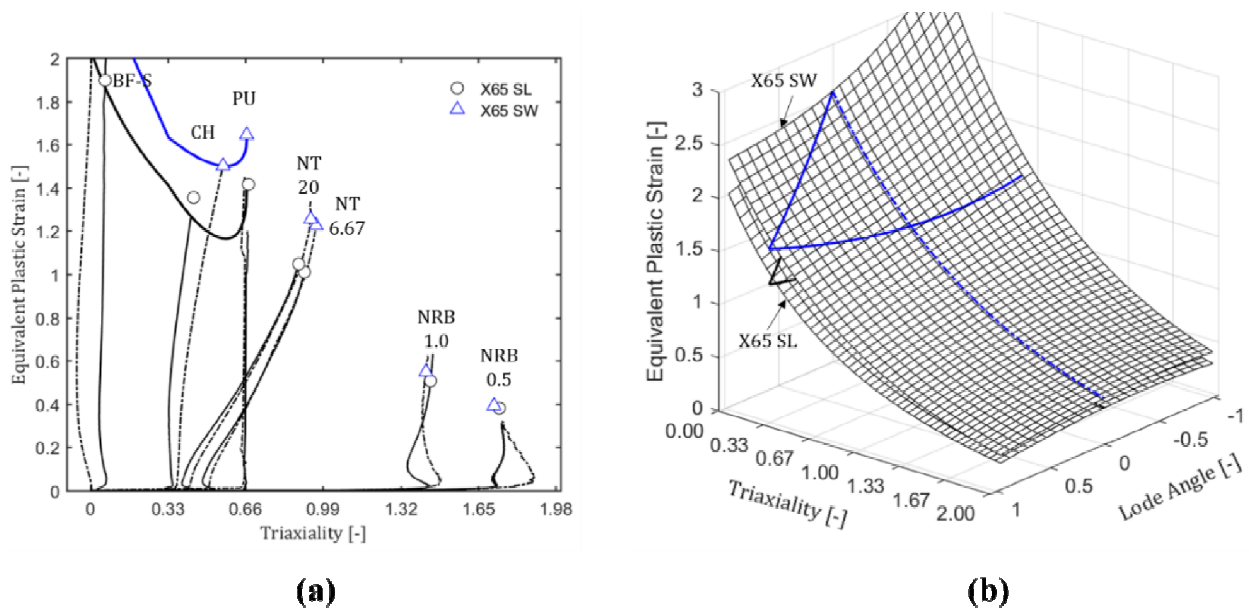(a)   (b)

Fig. 10 Comparison of (a) strain to fracture loading paths and (b) fracture surfaces of X65 pipeline steels. The open triangle symbols correspond to the estimated fracture initiation point, while the end of solid lines represent the strain to fracture computed through the hybrid experimental-numerical analysis.

Fig. 11 depicts the simulated mechanical response of selected FE models, which includes the experimental strain to fracture (solid triangle). In order to compare the load-deflection curves of both X65 steels, the nominal stress-strain is used to characterize mechanical response of the material all the way to fracture. The tensile stress is computed by dividing the applied tensile load to the net cross section, while strain is obtained by relating the displacement with the gauge length (see subsection 2.2 for details). Likewise, the measured fracture initiation points were converted into stress-strain notation as shown in Fig. 11. The outcomes show that the seamless pipe material exhibits a lower nominal yield stress regarding its seam weld counterpart, but it hardens significantly as deformation continues reaching the peak load approximately at the half

of the total nominal strain, specially, for flat tensile specimens, where stress triaxiality is less intense. However, X65-SW flow curves soften largely after the peak load, being the less ductile those configurations aligned with the reference 0° and transverse 90° directions. The diagonal direction response hardens slightly more than its alternatives, which improves ductility. This is also observed in the remaining configurations, while transverse and longitudinal orientations keep similar fracture state. A similar trend, but less significative, is observed for high triaxiality specimens where plastic and fracture anisotropy are comparable among materials.
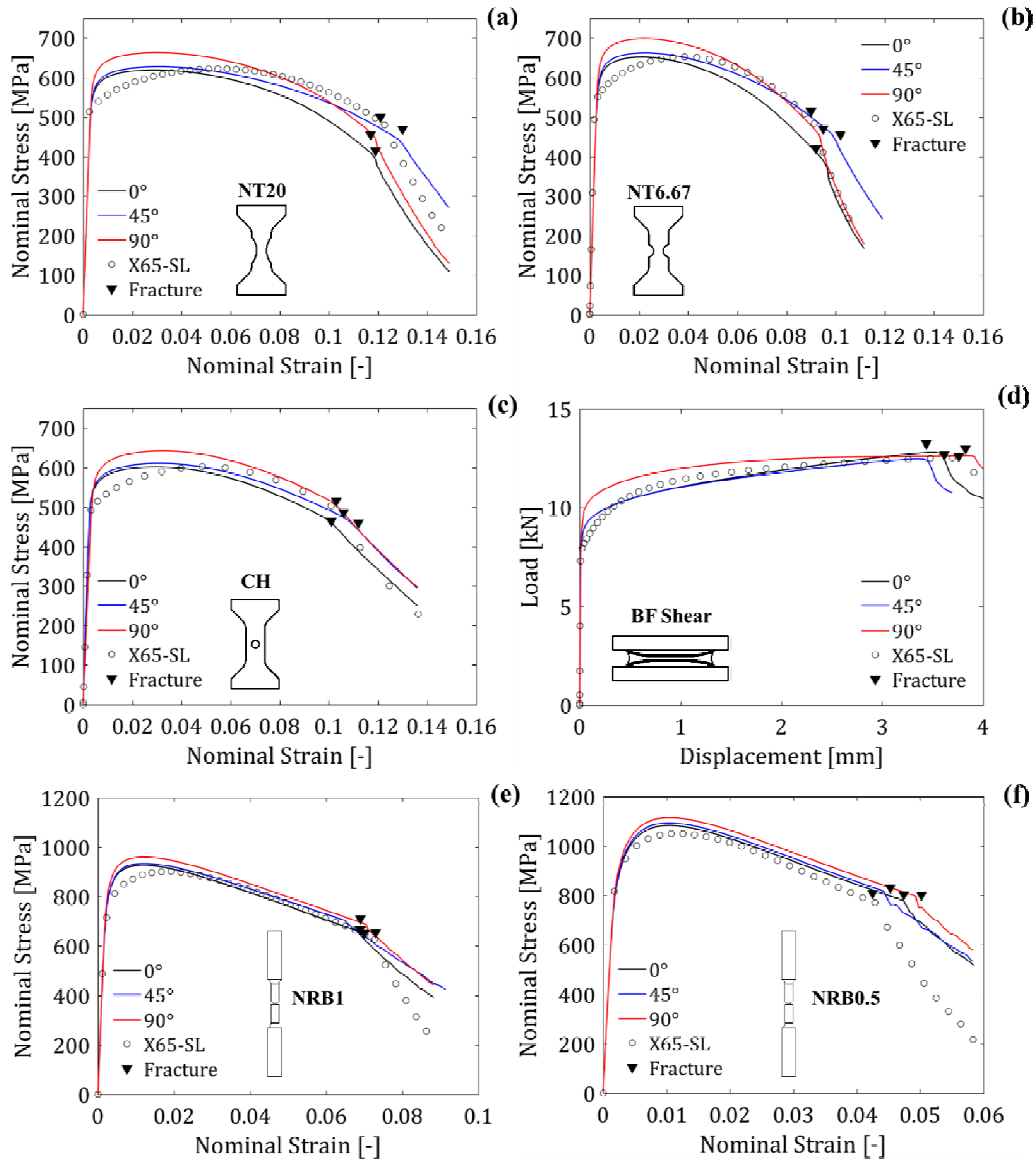

Fig. 11 Numerical simulations of load-deflection (nominal stress-strain) curves for X65 pipeline steels: (a) NT20; (b) NT6.67; (c) CH; (d) BF; (e) NRB1 and (f) NRB0.5. Colored lines and open circles correspond to simulated X65-SW and X65-SL, respectively. Solid marks (▼) are the measured fracture initiation points.

22

6. Discussion

It is important to point out that the approach presented herein is based purely on the idealistically proportional (linear) behavior of the evolving state variables controlling the facture process. Under such circumstance, the relation one-to-one between equivalent plastic strain and loading parameters $(\eta, \bar{\theta})$ holds all the way to fracture and its failure locus is unmistakably determined (Benzerga et al., 2012; Roth and Mohr, 2016). In practice, experiments under finite strain deform plastically up to the point where local stress state ceases to be proportional with the intended monotonically applied load and thus the fracture criterion adopted here might be fall apart. General non-proportional strain path is usually handled by time-weighted average values of some loading parameters such as stress triaxiality or Lode angle. Depending on the definition of these variables with respect to plastic strain (local or global) and the way they are computed experimentally or numerically, different fracture loci might be obtained (Basu and Benzerga, 2015). Indeed, this asseveration falls apart if the condition of radiality (proportionality) persists far beyond necking and fracture initiation becomes intrinsically part of the state of stress. In that sense, Thomas et al. (Thomas et al., 2016) performed a series of analyses on a family of non-linear loading paths to determine the strain-to-fracture loci with respect to stress triaxiality. Even though that work sheds some lights on the effects of strain history on the fracture process, it is limited to void growth fracture mechanism $(\eta > {}^{1}\!/_{3})$ with pre-straining settings followed by step jumps/downs. Such conditions differ strongly from what is observed in typical monotonically loading conditions, where local non-radiality is preceded by proportional loading after a short smooth transition stage. The notched flat NT's configuration is the perfect example of this behavior, where its strain history become non-proportional right after necking. From the micromechanics point of view, low-to-intermediate stress triaxiality levels are characterized by void distortion with negligible volumetric change as it is observed in fracture morphology after visual inspection. The dominated failure mechanism is shearing accompanied by some mixing parts of equiaxed dimples (Luo et al., 2012; Paredes et al., 2016). This proves to a certain extent, that fracture may initiates in the region where a secondary shear band forms and plastic instability occurs at intervoid ligaments. Thus, extracting the history of the stress state from the critical material point may induce an erroneous interpretation of the strain to fracture, which may be more related to structural instability rather than to the fracture process itself. As result, the saddle region ($\bar{\theta} = 0$ – see Fig. 10b –) characterized by lower ductility, typically observed in plane strain and generalized shearing conditions, ends up being comparable with its alternatives CH and PU. It is clear that the underlying fracture criterion relies upon the experiments solely, whose range of applicability falls on the stress state considered in the present study.

7. Concluding remarks

The mechanical characterization of X65 steels was carried out through a comprehensive experimental and numerical program to determine plastic and fracture behavior in two similar pipeline steels coming from different manufacturing process. The analysis shows that despite the differences found in plastic flow due to anisotropy, fracture initiation in both metals are comparable. It is clear that the material from the cold-working forming process exhibits yield

stress variations at different material orientation being the maxima along the transverse direction. It should also be noted that X65-SW displays a short uniform strain deformation compared to X65-SL, which directly impacts the plastic flow of the material. For instance, X65-SL hardens as deformation increases for large range, while X65-SW softens right after maximum stress is reached as shown in Fig. 11. This is more evident for tensile flat specimens, where the low stress triaxiality acting on the material point promotes necking and geometry changes at large plastic deformation. A rather different behavior is observed in notched bars, since it decouples plastic instability such as necking and shear banding from fracture. Thus, the influence of anisotropy is negligible. The triaxiality can be made wider by varying the notch radius, and crack propagation can be controlled.

It may conclude that the proposed anisotropic quadratic yielding function along with a non-associated flow rule enables the construction of a stress state dependent fracture envelope by inverse engineering method. The loading history extracted from the critical material point for each geometry provides the necessary information to construct the strain limit surface as function of η and $\bar{\theta}$ under proportional loading. The MMC provides the means to accommodate a wide range of stress state and loading modes.

Appendix A. Numerical procedure and FE models

A detailed 3D finite element models were developed for numerical analysis for all specimen geometries selected. Exploiting symmetry conditions of them only 1/8 of tensile specimens and ½ of special butterfly specimen were modeled. Orthogonal symmetric planes of FE models were constrained with zero normal displacement. A typical FE model is shown in Fig. A1 of a NRB specimen with two different radii. The model is meshed with trilinear eight cubic elements (C3D8R from Abaqus library) with reduced integration and hourglass control, being the more refined those allocate in the critical region near the center specimen with a characteristic length of 200µm. Monotonic quasi-static loading conditions are applied on each FE model similar to those conditions imposed on tests. The principal axes of anisotropy are assumed to be aligned with the material coordinates, in this case the pipe, such as: longitudinal (e_1 - 0°), hoop (e_2 - 90°) and through thickness (e_3) direction.

The constitutive model of plasticity and fracture was implemented into a VUMAT user-defined subroutine. Explicit time integration scheme with finite strain setting is employed for taking account nonlinear geometric changes and mass scaling factor to reduce computation time.
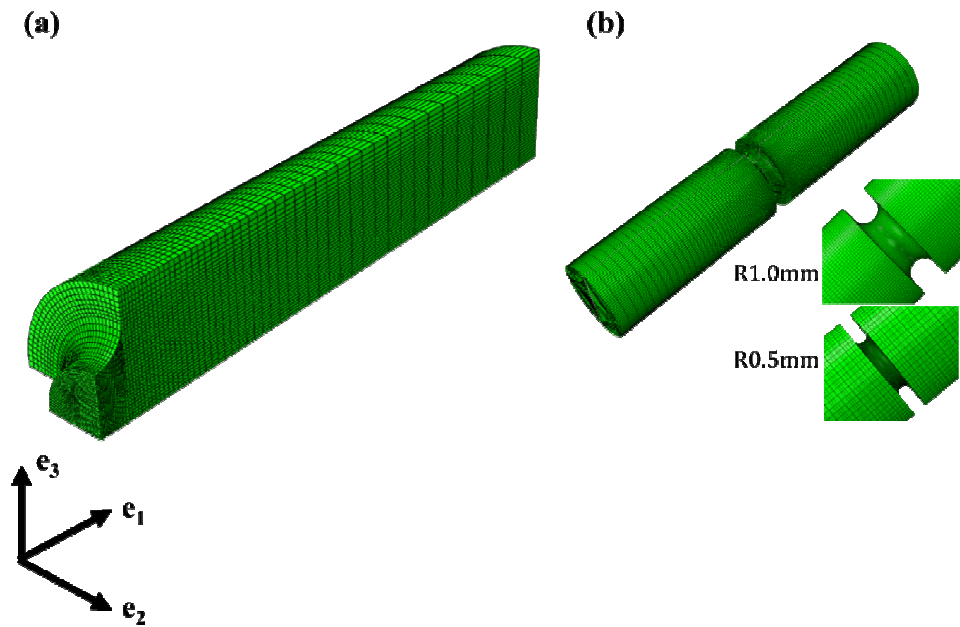

Fig. A1 (a) Quarter of FE model of NRB1 configuration; (b) Fully 3D representation of NRB's with different notch radii.

25

Appendix B. The state of stress characterization

The stress triaxiality (η) and the Lode angle ($\bar{\theta}$) parameters are defined in terms of the invariants of the Cauchy stress tensor $\boldsymbol{\sigma}$ in the form

$$\eta = \frac{\sigma_m}{\bar{\sigma}} \tag{B.1}$$

where, $\sigma_m = -\frac{1}{3} \operatorname{tr} \boldsymbol{\sigma}$ is the mean stress and $\bar{\sigma} = \sqrt{\frac{1}{2} \boldsymbol{S}:\boldsymbol{S}}$ is the von Mises equivalent stress. $\boldsymbol{S}$ stands for the deviatoric stress tensor, which is defined as

$$\boldsymbol{S} = \boldsymbol{\sigma} - (\operatorname{tr} \boldsymbol{\sigma})\mathbf{1} \tag{B.2}$$

$\mathbf{1}$ is the fourth order identity tensor. Likewise, the normalized Lode angle (simply called Lode angle) is represented as the normalized third invariant of the Cauchy stress deviator

$$\bar{\theta} = 1 - \frac{6\theta}{\pi}, \qquad -1 \le \bar{\theta} \le 1 \tag{B.3}$$

where θ is the actual Lode angle, which is defined as

$$\theta = \frac{1}{3}\cos^{-1}\left(\frac{27}{2} \frac{\det \boldsymbol{S}}{[\frac{1}{2}\boldsymbol{S}:\boldsymbol{S}]^{3/2}}\right), \qquad 0 \le \theta \le \pi/3 \tag{B.4}$$

The corresponding strain to fracture in plane stress condition is calculated by setting $\sigma_3 = 0$ and substituting into Eq. B.2 and Eq. B.4 to obtain a functional relation between the stress triaxiality and Lode angle parameter in the form

$$-\frac{27}{2}\eta\left(\eta^2 - \frac{1}{3}\right) = \sin\left(\frac{\pi}{2}\bar{\theta}\right) \tag{B.5}$$

References

Abi Akl Rami & Mohr Dirk (2017) 'Paint-bake effect on the plasticity and fracture of pre-strained aluminum 6451 sheets', *Mechanical Science*, 124–125, pp. 68–82. Available at: http://ac.els-cdn.com/S0020740317300218/1-s2.0-S0020740317300218-main.pdf?_tid=4a761a1a-10a3-11e7-b6a1-00000aacb362&acdnat=1490368097_fa4fbcdc076fe817d776341dfdacfbd4.

Arakawa, T. *et al.* (2013) 'Development of high performance UOE pipe for linepipe', *JFE Technical Report*, (18(Mar)), pp. 23–35. Available at: http://221.0.90.141.

Bai, Y. and Wierzbicki, T. (2008) 'A new model of metal plasticity and fracture with pressure and Lode dependence', *International Journal of Plasticity*, 24(6), pp. 1071–1096. doi: 10.1016/j.ijplas.2007.09.004.

Bai, Y. and Wierzbicki, T. (2010) 'Application of extended Mohr-Coulomb criterion to ductile fracture', *International Journal of Fracture*, 161(1), pp. 1–20. doi: 10.1007/s10704-009-9422-8.

Barlat, F., Lege, D. J. and Brem, J. C. (1991) 'A six-component yield function for anisotropic materials', *International Journal of Plasticity*, 7(7), pp. 693–712. doi: 10.1016/0749-6419(91)90052-Z.

Basu, S. and Benzerga, A. A. (2015) 'On the path-dependence of the fracture locus in ductile materials: Experiments', *International Journal of Solids and Structures*. doi: 10.1016/j.ijsolstr.2015.06.003.

Benzerga, A. ., Besson, J. and Pineau, A. (2004) 'Anisotropic ductile fracture', *Acta Materialia*, 52(15), pp. 4623–4638. doi: 10.1016/j.actamat.2004.06.020.

Benzerga, A. A. and Besson, J. (2001) 'Plastic potentials for anisotropic porous solids', *European Journal of Mechanics, A/Solids*, 20(3), pp. 397–434. doi: 10.1016/S0997-7538(01)01147-0.

Benzerga, A. A., Besson, J. and Pineau, A. (2004a) 'Anisotropic ductile fracture: Part I: Experiments', *Acta Materialia*, 52(15), pp. 4623–4638. doi: 10.1016/j.actamat.2004.06.020.

Benzerga, A. A., Besson, J. and Pineau, A. (2004b) 'Anisotropic ductile fracture: Part II: Theory', *Acta Materialia*, 52(15), pp. 4639–4650. doi: 10.1016/j.actamat.2004.06.019.

Benzerga, A. A. and Leblond, J. B. (2010) *Ductile Fracture by Void Growth to Coalescence*, *Advances in Applied Mechanics*. doi: 10.1016/S0065-2156(10)44003-X.

Benzerga, A. A., Surovik, D. and Keralavarma, S. M. (2012) 'On the path dependence of the fracture locus in ductile materials - Analysis', *International Journal of Plasticity*, 37, pp. 157–170. doi: https://doi.org/10.1016/j.ijplas.2012.05.003.

Broek, D. (1973) 'The role of inclusions in ductile fracture and fracture toughness', *Engineering Fracture Mechanics*, 5(1). doi: 10.1016/0013-7944(73)90007-6.

Bron, F. and Besson, J. (2004) 'A yield function for anisotropic materials Application to aluminum alloys', *International Journal of Plasticity*, 20(4–5), pp. 937–963. doi: 10.1016/j.ijplas.2003.06.001.

CIA (2014) *The World Factbook 2013-14*, *The World Factbook 2013-14*. Available at: https://www.cia.gov/library/publications/the-world-factbook/index.html.

Dunand, M. and Mohr, D. (2011) 'Optimized butterfly specimen for the fracture testing of sheet materials under combined normal and shear loading', *Engineering Fracture Mechanics*, 78(17), pp. 2919–2934. doi: 10.1016/j.engfracmech.2011.08.008.

Garrison, W. M. and Moody, N. R. (1987) 'Ductile fracture', *Journal of Physics and Chemistry of Solids*, 48(11), pp. 1035–1074. doi: 10.1016/0022-3697(87)90118-1.

Gu, G. and Mohr, D. (2015) 'Anisotropic Hosford-Coulomb fracture initiation model: Theory and application', *Engineering Fracture Mechanics*, 147, pp. 480–497. doi: 10.1016/j.engfracmech.2015.08.004.

Guo, B. *et al.* (2014) *Offshore Pipelines*, *Offshore Pipelines*. doi: 10.1016/B978-0-12-397949-0.00017-0.

Hara, T. *et al.* (2009) 'Metallurgical Design and Development of High Deformable High Strength Line Pipe Suitable for Strain-Based Design', *Isope*, 1, pp. 73–79.

Hara, T. *et al.* (2011) 'Development and Mass Production of X60 High Deformable Line Pipe Suitable for Strain-based Design', *Isope*, 8, pp. 575–580.

Herynk, M. D. *et al.* (2007) 'Effects of the UOE/UOC pipe manufacturing processes on pipe collapse pressure', *International Journal of Mechanical Sciences*, 49(5), pp. 533–553. doi: 10.1016/j.ijmecsci.2006.10.001.

Hill, R. (1949) 'The Theory of Plane Plastic Strain for Anisotropic Metals', *Proceedings of the Royal Society of London. Series A, Mathematical and Physical Sciences*, 198(1054), pp. 428–437. doi: 10.1098/rspa.1949.0110.

Iizuka, E., Hashimoto, K. and Kuwabara, T. (2014) 'Effects of anisotropic yield functions on the accuracy of forming simulations of hole expansion', in *Procedia Engineering*, pp. 2433–2438. doi: 10.1016/j.proeng.2014.10.346.

Institute, A. P. (2007) 'API 5L Specification for line pipe', *Api Spec 5L*, Forty Four, pp. 1–40. doi: 10.1520/G0154-12A.

Iob, F., Campanelli, F. and Coppola, T. (2015) 'Modelling of anisotropic hardening behavior for the fracture prediction in high strength steel line pipes', *Engineering Fracture Mechanics*, 148, pp. 363–382. doi: 10.1016/j.engfracmech.2015.04.030.

Jia, Y. and Bai, Y. (2016) 'Ductile fracture prediction for metal sheets using all-strain-based anisotropic eMMC model', *International Journal of Mechanical Sciences*, 115–116, pp. 516–531. doi: 10.1016/j.ijmecsci.2016.07.022.

Karafillis, A. P. and Boyce, M. C. (1993) 'A general anisotropic yield criterion using bounds and a transformation weighting tensor', *Journal of the Mechanics and Physics of Solids*, 41(12), pp. 1859–1886. doi: 10.1016/0022-5096(93)90073-O.

Ling, Y. (2004) 'Uniaxial True Stress-Strain after Necking', *AMP Journal of Technology*, 5(1), pp. 37–48.

Luo, M, Dunand, M, Mohr, D. (2012) 'Experiments and modeling of anisotropic aluminum extrusions under multi-axial loading – Part II: Ductile fracture', *International Journal of Plasticity*, 32–33, pp. 36–58. Available at: http://ac.els-cdn.com/S0749641911001896/1-s2.0-S0749641911001896-main.pdf?_tid=741afae0-14a2-11e7-b9c9-00000aacb360&acdnat=1490807542_9f4d9919bb5c35a050c1fcefd3c5069b.

Mohr, D., Dunand, M. and Kim, K. H. (2010) 'Evaluation of associated and non-associated quadratic plasticity models for advanced high strength steel sheets under multi-axial loading', *International Journal of Plasticity*, 26(7), pp. 939–956. doi: 10.1016/j.ijplas.2009.11.006.

Morgeneyer, T. F. *et al.* (2009) 'Experimental and numerical analysis of toughness anisotropy in AA2139 Al-alloy sheet', *Acta Materialia*, 57(13), pp. 3902–3915. doi: 10.1016/j.actamat.2009.04.046.

Paredes, M. *et al.* (2017) 'Ductile tearing analysis of TC128 tank car steel under mode I loading condition', *Theoretical and Applied Fracture Mechanics*. doi: 10.1016/j.tafmec.2017.10.006.

Paredes, M., Wierzbicki, T. and Zelenak, P. (2016) 'Prediction of crack initiation and propagation in X70 pipeline steels', *Engineering Fracture Mechanics*, 168. doi:

10.1016/j.engfracmech.2016.10.006.

Qian,L.,Fang,G., Zeng, P. (2017) 'Modeling of the ductile fracture during the sheet forming of aluminum alloy considering non-associated constitutive characteristic', *International Journal of Mechanical Science*, 126, pp. 55–66. Available at: http://ac.els-cdn.com/S0020740316304313/1-s2.0-S0020740316304313-main.pdf?_tid=e7feb1b2-1499-11e7-bc1f-00000aab0f02&acdnat=1490803871_223b1cfa3ca17890a073a6f8b2eaa25a.

Qian, L. *et al.* (2016) 'Experimental and numerical study on shear-punch test of 6060 T6 extruded aluminum profile', *International Journal of Mechanical Sciences*, 118, pp. 205–218. doi: 10.1016/j.ijmecsci.2016.09.008.

Rivalin, F. *et al.* (2000) 'Ductile tearing of pipeline-steel wide plates. II. Modeling of in-plane crack propagation', *Engineering Fracture Mechanics*, 68(3), pp. 347–364. doi: 10.1016/S0013-7944(00)00108-9.

Ronalds, B. F. (2005) 'Applicability ranges for offshore oil and gas production facilities', *Marine Structures*, 18(3), pp. 251–263. doi: 10.1016/j.marstruc.2005.06.001.

Roth, C. C. and Mohr, D. (2016) 'Ductile fracture experiments with locally proportional loading histories', *International Journal of Plasticity*, 79, pp. 328–354. doi: 10.1016/j.ijplas.2015.08.004.

Shinohara, Y., Madi, Y. and Besson, J. (2016) 'Anisotropic ductile failure of a high-strength line pipe steel', *International Journal of Fracture*, 197(2), pp. 127–145. doi: 10.1007/s10704-015-0054-x.

Van Stone, R. H. *et al.* (1985) 'Microstructural aspects of fracture by dimpled rupture', *International Metals Reviews*, 30(4), pp. 157–180. doi: 10.1179/imtr.1985.30.1.157.

Stoughton, T. B. (2002) 'A non-associated flow rule for sheet metal forming', in *International Journal of Plasticity*, pp. 687–714. doi: 10.1016/S0749-6419(01)00053-5.

Suh, Y. S., Saunders, F. I. and Wagoner, R. H. (1996) 'Anisotropic yield functions with plastic-strain-induced anisotropy', *International Journal of Plasticity*, 12(3), pp. 417–438. doi: 10.1016/S0749-6419(96)00014-9.

Tanguy, B. *et al.* (2008) 'Plastic and damage behaviour of a high strength X100 pipeline steel: Experiments and modelling', *International Journal of Pressure Vessels and Piping*, 85(5), pp. 322–335. doi: 10.1016/j.ijpvp.2007.11.001.

Thomas, N., Basu, S. and Benzerga, A. A. (2016) 'On fracture loci of ductile materials under non-proportional loading', *International Journal of Mechanical Sciences*. doi: 10.1016/j.ijmecsci.2016.08.007.

Tsuru, E. *et al.* (2008) 'Numerical Simulation of Buckling Resistance for UOE Line Pipes with Orthogonal Anisotropic Hardening Behavior', *Proceedings of the Eighteenth International Offshore and Polar Engineering Conference*, 8, pp. 104–110.

Tubb, M. (2001) 'International pipeline construction outlook: Oil & gas infrastructure', *Pipeline & Gas Journal*, 228(8), p. 16. Available at: http://search.proquest.com/docview/197489021?accountid=47173%5Cnhttp://uf2mu7dg8q.search.serialssolutions.com/?ctx_ver=Z39.88-2004&ctx_enc=info:ofi/enc:UTF-8&rfr_id=info:sid/ProQ%3Asciencejournals&rft_val_fmt=info:ofi/fmt:kev:mtx:journal&rft.genre=article.

Wierzbicki, T. and Xue, L. (2005) *On the Effect of the Third Invariant of the Stress Deviator on Ductile Fracture*, *Technical report, Impact amd Crashworthiness Laboratory, Massachusetts Institute of Technology, Cambridge, MA*. Technical report, Impact and Crashworthiness Laboratory,Cambridge, MA.